PNAS RESEARCH ARTICLE | ENGINEERING

Origin for electrochemically driven phase transformation in the oxygen electrode for a solid oxide cell

Emir Dogdibegovic[a], Yudong Wang[a,b,1], and Xiao-Dong Zhou[a,b,1]

Edited by Alexis Bell, University of California, Berkeley, CA; received February 28, 2022; accepted September 16, 2022

The next generation of fuel cells, electrolyzers, and batteries requires higher power, faster kinetics, and larger energy density, which necessitate the use of compositionally complex oxides to achieve multifunctionalities and activity. These compositionally complex oxides may change their phases and structures during an electrochemical process—a so-called "electrochemically driven phase transformation." The origin for such a phase change has remained obscure. The aim of this paper is to present an experimental study and a theoretical analysis of phase evolution in praseodymium nickelates. Nickelate-based electrodes show up to 60 times greater phase transformation during operation when compared with thermally annealed ones. Theoretical analysis suggests that the presence of a reduced oxygen partial pressure at the interface between the oxygen electrode and the electrolyte is the origin for the phase change in an oxygen electrode. Guided by the theory, the addition of the electronic conduction in the interface layer leads to the significant suppression of phase change while improving cell performance and performance stability.

electrochemically driven phase transformation | solid oxide cells | oxygen electrode | stability

Significance

Understanding the origin of phase transformation of an electrode during operation lies at the heart of elucidating the science behind the performance durability of fuel cells, electrolyzers, and batteries. It is known that electrode materials often undergo undesirable phase transformation at a high current density or under a high voltage. The aim of this article is to provide a fundamental understanding of the origin for phase transformation in oxygen electrodes during operation and use this knowledge to develop a high-performance electrode that exhibits improved performance stability.

Materials research for advanced energy systems (e.g., fuel cells, electrolyzers, and batteries) has been driven by the recognition that multifunctionalities in component materials are needed in order to achieve higher power density, faster kinetics, and larger energy density. For instance, mixed electronic and ionic conducting oxides are used as the electrode for the oxygen reduction reaction—a cathode—in a solid oxide fuel cell (SOFC). These complex oxides may change their phases and structures during an electrochemical operation—a so-called "electrochemically driven phase transformation." Schmalzried et al. (1) reported in 1979 an akin phenomenon in $(Co_{1-x}Mg_x)O$, called cation kinetic demixing. Cation kinetic demixing was attributed to the presence of thermodynamic potential gradients on $(Co_{1-x}Mg_x)O$, under which Co is a faster-moving component than Mg (1). Dimos and coworkers (2) further investigated (Co,Mg)O and yttrium-stabilized zirconia (YSZ) (3), and they carried out theoretical treatment (4) of kinetic demixing. In the absence of an electric field, assuming that anions and cations move independently, the Gibbs–Duhem relation gives $x_C d\mu_C + x_{O^{2-}} d\mu_{O^{2-}} = 0$, where μ is the chemical potential and x is molar fraction for the oxygen ion (O^{2-}) or a cation (C). If one cation in a material is more mobile than the other, the originally homogeneous material becomes inhomogeneous, indicating that kinetic demixing takes place (5). Petot-Ervas and Petot then investigated SOFC electrolytes (e.g., YSZ and Gd-doped ceria [GDC] under an electric field with Pt as the electrodes) (6). Kinetic demixing was observed in both YSZ and GDC under operating conditions. They proposed that transport processes on the cation sublattice play an important role on both the chemical properties and aging behavior of the electrochemical cells based on YSZ or GDC.

Cation kinetic demixing or in a broader sense, electrochemically driven phase transformation is more complex in an active oxygen electrode than in an electrolyte because both oxygen ions and electron holes move across the electrode in a substantial flux. As a consequence, local oxidation or reduction may take place along with possible kinetic cation demixing, phase transformation, amorphorization, or even a solid-state reaction. For instance, when $(La,Sr)(Fe,Co)O_3$ (LSCF) was used as a microelectrode with 80% Co, Baumann et al. (7) observed Sr and Co surface enrichment on dense electrodes, suggesting the kinetic demixing of Sr ions and possible Co ions. When LSCF was exposed under oxygen chemical potential gradients, kinetic demixing and decomposition of LSCF membranes were observed from the analysis of the microstructure and phase composition near the surfaces (8–11). This paper aims to provide a basic understanding of electrochemically driven phase transformation phenomena via studying the phase transformation of $(Pr_{1-x}Nd_x)_2NiO_4$ under various electrochemical conditions.

Author affiliations: [a]Department of Chemical Engineering, University of South Carolina, Columbia, SC 29065; and [b]Institute for Materials Research and Innovation, University of Louisiana at Lafayette, Lafayette, LA 70592

Author contributions: E.D. and X.-D.Z. designed research; E.D. and Y.W. performed research; E.D., Y.W., and X.-D.Z. analyzed data; and E.D., Y.W., and X.-D.Z. wrote the paper.

The authors declare no competing interest.

This article is a PNAS Direct Submission.

[1]To whom correspondence may be addressed. Email: yudong.wang1@louisiana.edu or zhou@louisiana.edu.

Published November 2, 2022.

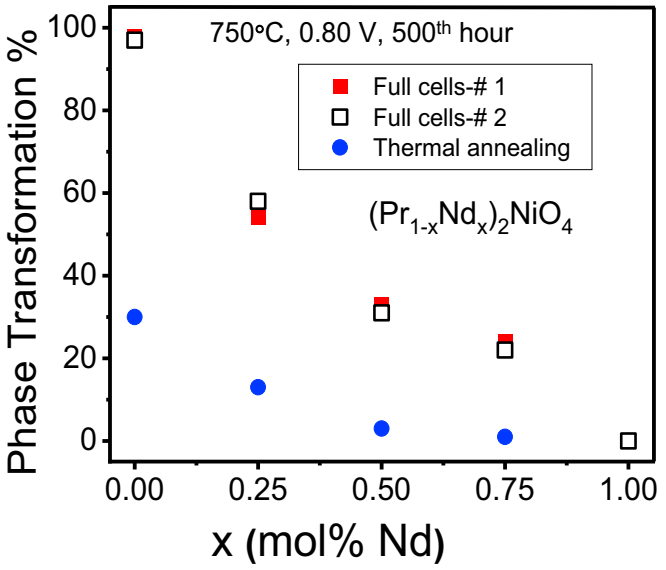

Fig. 1. Phase evolution in thermally annealed electrodes (750 °C, 500 h) and electrochemically operated $(Pr_{1-x}Nd_x)_2NiO_4$ electrodes after 500 h at 750 °C and 0.80 V.

Results

The $(Pr_{1-x}Nd_x)_2NiO_4$ (PNNO)-based oxygen electrode undergoes phase transformation into a Pr_6O_{11} (PrO_x) phase and a higher-order $Pr_3Ni_2O_{7+\delta}$ phase at SOFC operation temperatures (12). Fig. 1 shows the quantified phase transformation in PNNO electrodes that were treated with either thermally annealing or electrochemically operating in full cells at 750 °C for 500 h. The quantification method of phase transformation was reported previously (13). Two sets of full cells show reproducible phase transformation, as shown in Fig. 1. The percentage of phase transformation in thermally annealed electrodes is substantially lower than in operated electrodes. Clearly, accelerated phase transformation exists during an electrochemical operation.

Since the phase transformation in operating nickelate electrodes has rarely been reported, this discrepancy is not yet addressed in the open literature. The parent compound without Nd substitution ($x = 0$ in Fig. 1), Pr_2NiO_4 (PNO), is a known active oxygen electrode, which undergoes phase transformation during a thermally annealing process (12–16). The percentage of phase transformation in Pr_2NiO_4 was ~30% in an electrode annealed at 750 °C for 500 h. It, however, reached to nearly 100% when Pr_2NiO_4 was used as the cathode in a full cell at 750 °C for 500 h at 0.8 V. Two separated cells were examined, and results were highly reproducible for all cathodes measured as a function of x in $(Pr_{1-x}Nd_x)_2NiO_4$. With an increase in x, the phase transformation is suppressed, and it was fully suppressed in Nd_2NiO_4 ($x = 1$) (16).

Fig. 1 brings into a question the extent to which operating conditions influence the phase transformation in nickelate-based oxygen electrodes. In order to establish the relationship between structural changes and cell operation, the phase transformation was studied as a function of operating temperatures and current densities. First, baselines were developed, including the cathode before operation and thermally annealed electrodes. Fig. 2*A* shows that the operation of $(Pr_{0.50}Nd_{0.50})_2NiO_4$ (PNNO50-50) at 700 °C and 0.10 A/cm^2 for 300 h does not lead to phase transformation, as shown by the preserved parent phase. However, once the current density is raised to 0.50 A/cm^2, a clear phase evolution follows with the formation of PrO_x (+ in Fig. 2*A*). Therefore, the phase transformation indeed results from the electrochemical operation and must not be overlooked when quantifying phase evolution in an SOFC cathode. A systematic study at various temperatures and current densities was then carried out to understand electrochemically driven phase transformation.

As shown in Fig. 2*B*, phase transformation was accelerated at 750 °C at both 0.10 and 0.50 A/cm^2. With an increase in current density, the phase transformation increases (17–19). Similarly, the electrochemical operation in full cells at 790 °C leads to major phase transformation at 0.50 and 0.75 A/cm^2, as shown in Fig. 2*C*. On the other hand, thermally annealed PNNO50-50 powders (between 700 °C and 790 °C) do not exhibit any significant phase transformation after 300 h, consistent with the results shown in Fig. 1. In fact, only ~1 mol % of PrO_x is formed after 300 h of annealing at 790 °C (Fig. 2*C*).

Fig. 3 summarizes quantified phase transformation in thermally annealed PNNO50-50 powders and electrodes along

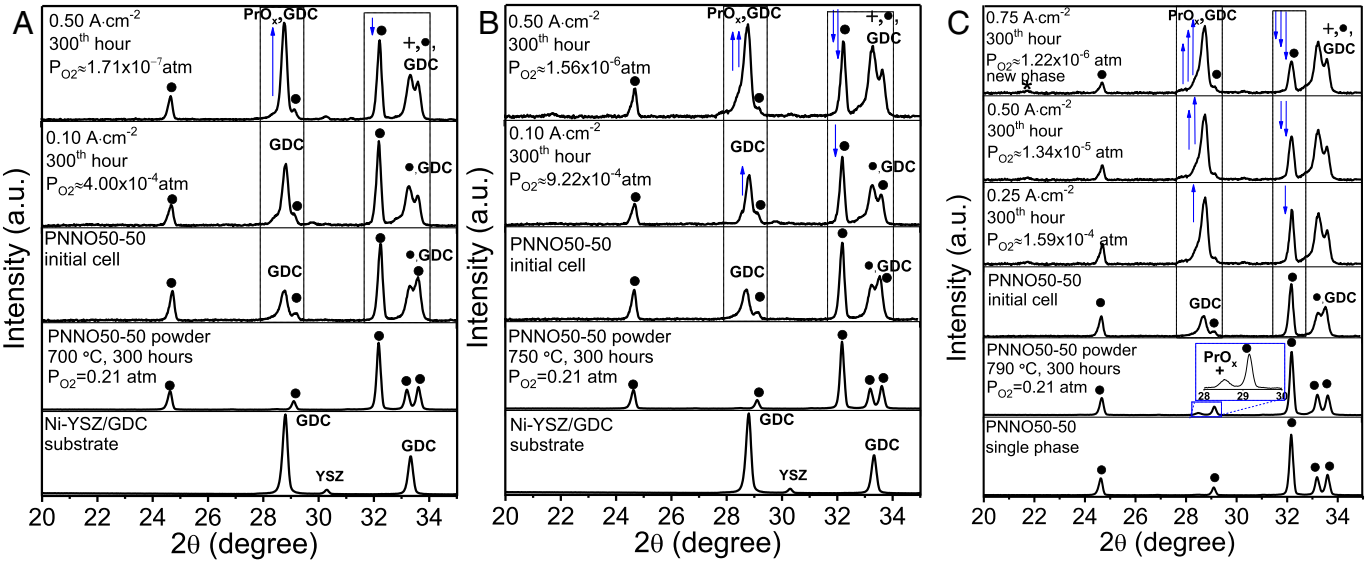

Fig. 2. Phase evolution in PNNO electrodes operated under different current densities at (*A*) 700 °C, (*B*) 750 °C, and (*C*) 790 °C. Standard X-ray diffraction (XRD) patterns for the Ni-YSZ/GDC substrate and PNNO powder are shown in *A* and *B*. The peaks of PrO_x, PNNO, and $Pr_3Ni_2O_7$ phases are marked as "+", "•" and "*", respectively.

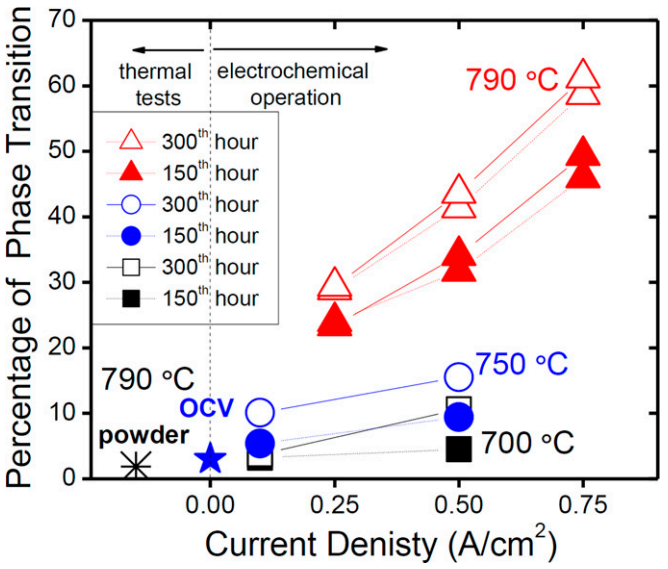

Fig. 3. Quantified phase transformation in PNNO powders and electrodes. Powders and electrodes at open circuit voltage (OCV) were thermally annealed at 790 °C for 500 h in air. Phase evolution in electrochemically operated electrodes is illustrated as a function of current density at various temperatures and operating times.

with electrochemically operated cathodes. The plot was divided into two regions: 1) a region of thermally driven phase transformation and 2) a region of electrochemically driven phase changes. After 500 h of annealing at 790 °C, both powders and electrodes (YSZ/GDC/PNNO configuration) show only a few percentages of phase transformation. A 1 to 2% larger phase transformation in electrode was detected due to the previously discussed reaction with the GDC interlayer (16). However, it is clear that the electrochemical operation significantly accelerates phase transformation in nickelates. At 700 °C, the PNNO50-50 electrodes operated at 0.50 A/cm^2 undergo 10.6% phase transformation. With a further increase in temperature, the phase transformation reached 15.5% at 750 °C and 0.50 A/cm^2. Even more evident results were obtained at 790 °C, where phase transformation was 60 times larger than in thermal annealing studies at the same temperature. While the operation at a mild condition, 0.10 A/cm^2 and 700 °C, exhibited zero phase transformation, increased temperature and operating time do show accelerated phase transformation, further indicating the role of the electrochemical operation in the phase evolution.

Discussion

To understand the origin for electrochemically driven phase transformation, a theoretical analysis is provided (vide infra). It is known that much of our understanding of physical behavior of materials is based on the concept of local thermodynamic equilibrium, which is at the heart of classical thermodynamics and modern reaction kinetics (20–22). Based on the local thermodynamic equilibrium assumption, the equation $O_2(\vec{r}) + 4e^-(\vec{r}) \leftrightarrow 2O^{2-}(\vec{r})$ is valid in both SOFC electrolyte and electrodes, where $\vec{r}$ is any position in the system. The assumption of local thermodynamic equilibrium implies $\mu_{O_2}(\vec{r}) + 4\tilde{\mu}_e(\vec{r}) = 2\tilde{\mu}_{O^{2-}}(\vec{r})$, where μ denotes the chemical potential and $\tilde{\mu}$ represents the electrochemical potential of a species. The analysis suggests that the existence of a chemical potential of oxygen as a gas in a fully dense solid is appropriate.

Nonzero electronic current is a key implication of the local thermodynamic equilibrium assumption, which implies that even in a predominantly ionic conductor, the electronic current cannot be entirely neglected. This is because the electronic transport, however small, plays a decisive role in the establishment of the above equilibrium and thus, in the establishment of the local chemical potential of oxygen, $\mu_{O_2}(\vec{r})$, which in turn, dictates the stability of an electrode. In terms of electronic current density, I_e, and ionic current density, I_i, through the electrolyte, the chemical potential of oxygen, μ_{O_2}, at the cathode/electrolyte interface, $\mu^c_{O_2}$, is given by (20) $\mu^c_{O_2} = \mu^{cathode}_{O_2} + 4e(r^c_i I_i - r^c_e I_e)$, where $\mu^{cathode}_{O_2}$ is the μ_{O_2} in the cathode gas, r^c_i is the ionic interfacial area–specific resistance (ASR) at the cathode/electrolyte interface, and r^c_e is the electronic interfacial ASR at the cathode/electrolyte interface.

Assuming the ideal gas law for oxygen, one can obtain $\mu^{cathode}_{O_2} = \mu^o_{O_2} + k_B T \ln(P^{cathode}_{O_2})$, where $\mu^o_{O_2}$ is standard-state gas phase oxygen chemical potential and $P^{cathode}_{O_2}$ is the oxygen partial pressure at the cathode (gas phase). Then, $P^c_{O_2} \approx P^{cathode}_{O_2} \exp[-\frac{4e(r^c_i|I_i| + r^c_e|I_e|)}{k_B T}]$, suggesting that the oxygen partial pressure of the interface between the oxygen electrode and electrolyte, $P^c_{O_2}$, is less than $P^{cathode}_{O_2}$, which is the oxygen partial pressure of the incoming oxidant (e.g., 21% in air). In order to estimate the possible magnitude of $P^c_{O_2}$, numerical estimates are presented in what follows for assumed values of parameters. The magnitude of the pressure difference is dependent upon the $(r^c_i|I_i| + r^c_e|I_e|)$. Let the operating temperature be 800 °C (1,073 K), and assume that $(r^c_i|I_i| + r^c_e|I_e|) = 0.2$ V, suggesting that the cell potential difference at the cathode is 0.2 V. Then, with air as the oxidant ($P^{cathode}_{O_2} = 0.21$ atm), the estimated $P^c_{O_2} \approx 3.7 \times 10^{-5}$ atm, a reducing environment that can indeed change the phase stability of a cathode. The local oxygen partial pressure (the level of reducing condition) depends on both $r^c_i|I_i|$ and $r^c_e|I_e|$. The most reducing location is at the immediate cathode/electrolyte interface. Table 1 lists the magnitude of $P^c_{O_2}$ as a function of cathodic potential difference. The greater $P^c_{O_2}$ is, the more stable the cathode is during operation. If the cathode potential difference is 0.4 V, the local $P^c_{O_2}$ is as low as 6.5×10^{-9} atm, at which both LSCF and nickelates will go through a phase change. In a real case, however, the ionic current can be measured directly, while it is challenging to obtain the r^c_e and I_e. By considering the total electrical potential drop across the cell ($V_{cell} = r^t_e|I_e|$), the oxygen partial pressure can be calculated by $P^c_{O_2} = P^{cathode}_{O_2} \exp\left[-\frac{4e}{k_B T}\left(r^c_i|I_i| + \frac{r^c_e}{r^t_e} V_{cell}\right)\right]$. The ratio, $\frac{r^c_e}{r^t_e}$, represents the fraction of cathode electronic resistance (r^c_e) to the total electronic resistance (r^t_e), which is ~0.06 because the r^t_e is dominated by the electronically insulative electrolyte (23). The cathode ionic resistance, r^c_i, can be estimated from the distribution of relaxation time analysis (24–26). As the result, $P^c_{O_2}$ values are estimated and listed in Fig. 2.

As shown in the above discussion, one way to improve the local P_{O_2} at the cathode/electrolyte interface is to reduce the electronic resistance by introducing electronic conduction into the interlayer: for instance, the presence of Pr (27). Fig. 4*A*

Table 1. Oxygen partial pressure ($P^c_{O_2}$) at the cathode/electrolyte interface as a function of the potential difference at the oxygen electrode

Potential difference	0.05 V	0.1 V	0.2 V	0.3 V
$P^c_{O_2}$ (atm)	0.024	0.0029	3.7×10^{-5}	4.9×10^{-7}

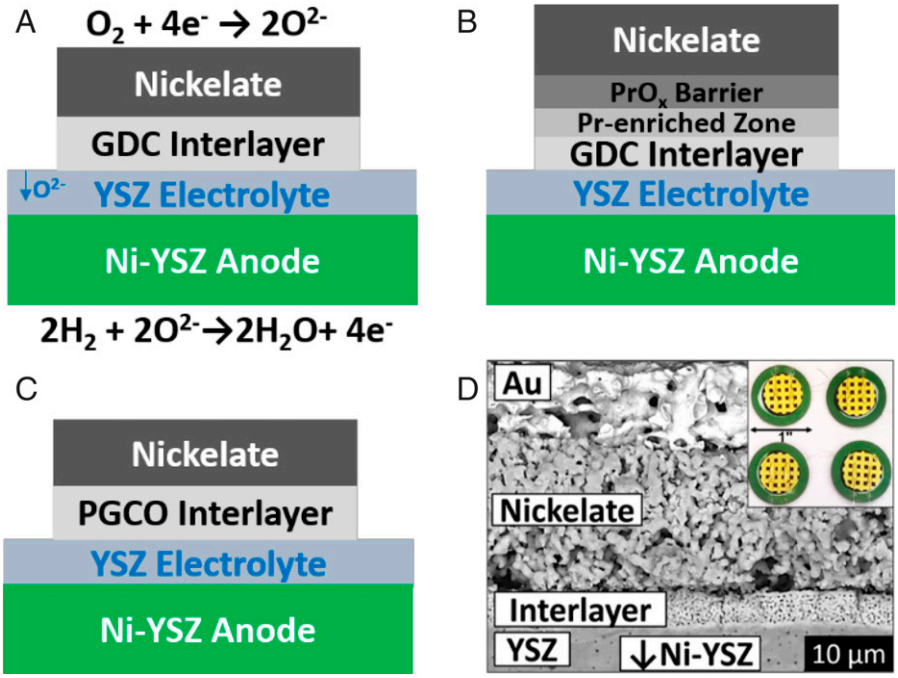

Fig. 4. Schematics showing the overall electrochemical reaction in fuel cells and a nickelate electrode printed on (*A*) GDC20 (*B*) PrO_x–GDC, and (*C*) PGCO interlayers in full cell configuration. (*D*) Representative scanning electron microscope (SEM) image of a cell cross-section showing the respective thickness of each layer. A top view of the Au grid (*Inset*) is shown, which provides an exposure window for phase quantification studies. Nickelate represents PNO or PNNO.

illustrates a standard cell configuration with a conventional $Gd_{0.20}Ce_{0.80}O_{1.90}$ (GDC20) interlayer. The first approach to design interlayers involved a deposition of a thin Pr_6O_{11} film (~0.2 μm) on the top of GDC20 (named as PrO_x–GDC) with a Pr-enriched zone at the boundary after sintering, as shown in Fig. 4*B*. The second approach is to tune the interlayer chemistry by using Pr/Gd codoped ceria $Pr_{0.10}Gd_{0.10}Ce_{0.80}O_{1.90\pm\delta}$ (PGCO), a bulk form rich with Pr, as shown in Fig. 4*C*. Table 2 summarizes the materials and their functions in this study. These cell configurations were then used to study the role of the interlayer on the phase transformation and performance stability of the cathodes (17–19). Fig. 4*D* shows a scanning electron microscope image of a cell cross-section, illustrating a respective thickness of each layer and a gold grid current collector, which allows for accurate phase evolution studies in cathodes (12).

Fig. 5, *Left* shows the current density as a function of time for PNO cathodes on various interlayers at 0.8 V. For each condition, two cells were measured. The results are reproducible and consistent among all cells. Remarkable performance stability was observed in cells with the PGCO interlayer, with 0% degradation during 500-h tests. Furthermore, the current density at 750 °C and 0.80 V was promoted by 27% (1.4 A/cm^2) with PGCO, in comparison with the use of a conventional GDC interlayer.

Table 2. A list of the materials, their chemical compositions, and their functions

Material	Chemical composition	Function
PNO	$Pr_2NiO_{4+\delta}$	Oxygen electrode
PNNO	$(Pr_{1-x}Nd_x)_2NiO_{4+\delta}$	Oxygen electrode
PNNO50-50	$(Pr_{0.5}Nd_{0.5})_2NiO_{4+\delta}$	Oxygen electrode
GDC	$Gd_xCe_{1-x}O_{2-0.5x}$	Interlayer
GDC20	$Gd_{0.20}Ce_{0.80}O_{1.90}$	Interlayer
PGCO	$Pr_{0.10}Gd_{0.10}Ce_{0.80}O_{1.90}$	Interlayer

With a conventional GDC interlayer, the decreases in fuel cell performance originate from the decomposition of the Pr_2NiO_4 phase (28). The cells with the PrO_x–GDC interlayer exhibited better performance stability than those with the conventional GDC. The decrease in r_e^c leads to a smaller oxygen chemical potential gradient at the electrode/electrolyte interface ($r_e^{c,PGCO} < r_e^{c,PrO_x-GDC} < r_e^{c,GDC}$). As a result, the less reductive atmosphere with a mild $P_{O_2}^c$ value ($P_{O_2}^{cathode} > P_{O_2}^{c,PGCO} > P_{O_2}^{c,PrO_x-GDC} > P_{O_2}^{c,GDC}$) suppresses the phase transition in the nickelate electrode so that the high performance is preserved.

Fig. 5, *Right* shows similar findings for the PNNO50-50 electrodes. Doping Nd into the Pr_2NiO_4 structure aims to improve the phase stability of the oxygen electrode (16, 29). A high performance with nearly zero degradation at 750 °C and 0.80 V was achieved with a PGCO interlayer. The consistent and reproducible measurements in multiple cells for each interlayer configuration and electrode composition indicate the reliability of our experimental approaches. What surprised us is that the performance of both PNO and PNNO50-50 exhibit significantly improved performance stability over a 500-h operation on the PGCO layer. This is contradicted by an enduring assumption that the higher the activity, the less the performance stability. The observation of a high-performance and highly stable cathode is, however, consistent with the theoretical analysis.

To further illustrate the relation between the phase transformation and electrochemical operation with different interlayers, Fig. 6*A* shows the phase evolution in PNO cathodes in operated full cells, as shown in Figs. 4 and 5*A*. With GDC20, 45% of phase decomposition occurs, confirmed by evolution or PrO_x (+ in Fig. 6*A*) and a higher-order $Pr_3Ni_2O_7$ phase (* in Fig. 6*A*). However, the cells with the PGCO layer provide the most promising results. After 500 h of electrochemical operation, the majority (87%) of the PNO phase (• in Fig. 6*A*) was preserved, which agrees with the better performance stability of the cell with PGCO than the one with GDC. In addition, the

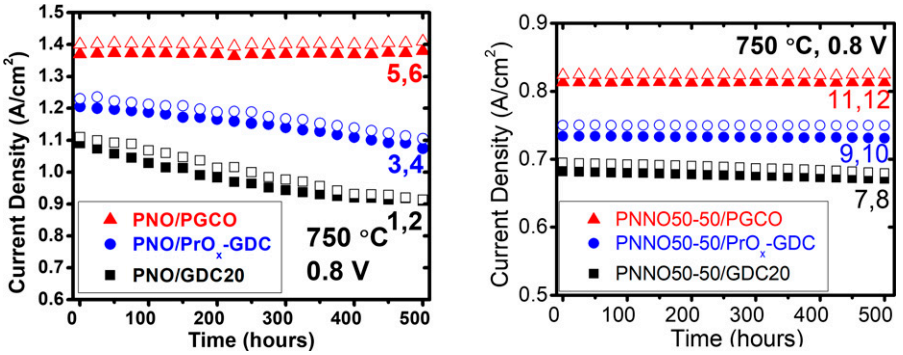

Fig. 5. Electrochemial performance vs. time for (*Left*) PNO and (*Right*) PNNO full cells operated at 750 °C and 0.80 V. Two cells per each condition are shown. PGCO stands for $(Pr_{0.1}Gd_{0.1})Ce_{0.8}O_{1.9}$, as shown in Fig. 4*C*. PrO_x–GDC corresponds to the configuration in Fig. 4*B*.

PNNO cathode retained a completely stable structure with the PGCO interlayer (the initial ratio of peak intensities was preserved), as shown in Fig. 6*B*. If a conventional GDC20 was used, despite the absence of the formation of the $Pr_3Ni_2O_7$ phase in PNNO electrodes, the evolution of the PrO_x peak ($2\theta \sim 29°$) is a clear indication of phase change. These results establish a correlation between phase transformation and electrochemical operation. A proper selection of the interlayer does play a significant role in stabilizing the parent phase. In operando XRD analysis in full cells at 750 °C and 0.80 V (Fig. 6*C*) confirms that the active phase at high current densities ($i \geq 1.0$ A/cm^2) is the prevalent high-temperature nickelate phase. PrO_x was not formed in the PNNO50-50 electrode after 150 h of electrochemical operation.

In summary, when an oxygen electrode is under polarization, the oxygen partial pressure at the interface between the oxygen electrode and the electrolyte is lower than that of incoming oxidant. Under high polarization, the environment at the aforementioned interface leads to the phase transformation of the oxygen electrode. The local oxygen partial pressure is determined by the transport properties at the interfaces. The addition of electronic conduction in the interface layer results in improved cell performance and performance stability, while the phase transformation is significantly suppressed.

Materials and Methods

Thermogravimetric analysis was used to standardize raw materials, including $Pr(NO_3)_3 \cdot xH_2O$, $Nd(NO_3)_3 \cdot xH_2O$, and $Ni(NO_3)_2 \cdot xH_2O$ (99.9% REO; Alfa Aesar). The glycine–nitrate combustion process was adopted to synthesize nickelate powders (30), which were then calcined in air at a heating and cooling rate of 3°C/min. Phase analysis was carried out by using an X-ray diffractometer (Rigaku Miniflex II), which was equipped with scintillating and high-speed silicon strip (D/teX) detectors. We have reported details to normalize the flux and peak positions by using multiple external and internal standards (13). All thermal annealing processes took place in 3% humidified airflow (18).

Details on cell fabrication procedures are reported elsewhere (13, 31). In brief, anode-supported button cells (1-inch diameter) were used for electrochemical measurements. The interlayer between the oxygen electrode and YSZ electrolyte consisted of a bimodal doped ceria GDC20, which was screen printed. The doped ceria interlayer was then sintered at 1,200 °C for 2 h together with the anode current collector composed of Ni paste and Pt wires imbedded into Ni mesh. Micrometer carbon powders were added to cathode powders as a pore former. The mixture of carbon and cathode powders was then ball milled to obtain a mean particle size of 270 ± 60 nm (obtained via SEM

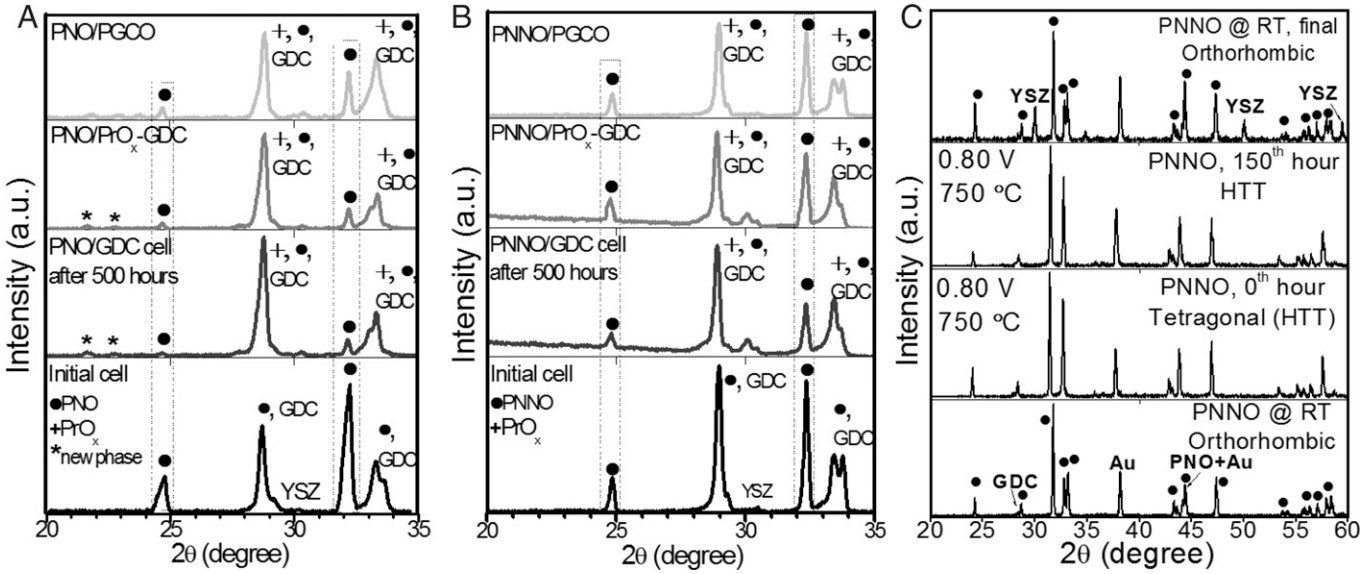

Fig. 6. Phase evolution in (*A*) PNO and (*B*) PNNO50-50 electrodes operated in full cells at 750 °C and 0.80 V. The flux was normalized, and peak positions were calibrated with multiple external (Ni-YSZ, single-phase PNO and PrO_x) and internal (Au) standards. An XRD pattern illustrated along the bottom shows the initial cathode/GDC/YSZ/Ni-YSZ cell. Shown progressively from the bottom to the top are the final XRD patterns on cells with various interlayers. The cells with the PGCO interlayer show a preserved nickelate phase. (*C*) In situ XRD patterns on an operating PNNO electrode. Phase transformation from room temperature (RT) orthorhombic phase to high-temperature tetragonal (HTT) phase occurs at operating conditions. The parent nickelate phase in PNNO was fully preserved after the operation. The peaks of PrO_x, nickelates, and $Pr_3Ni_2O_7$ phases are marked as "+", "•" and "*", respectively.

and a particle size analyzer) to prepare cathode ink (18). The ink was screen printed and sintered at 1,200 °C for 2 h, resulting in a 25-μm electrode thickness with an active area of 2 cm^2. A gold metal grid was screen printed and sintered at 900 °C to function as the cathode current collector (13, 31). Two Pt wires were cosintered with gold grids, which allows for the four-probe measurements.

Each button cell was sealed on a tubular alumina stand with a glass paste. A perforated alumina cap was placed on top of the cell and spring-loaded to provide sufficient mechanical contact and air delivery to the cathode side. All button cells were electrically connected with a potentiostat with Pt wires. During the electrochemical measurements, the anode side was provided with 3% humidified H_2 at a flow rate of 200 sccm, while the cathode side was supplied with 400-sccm air. The current density-voltage (i-V) sweep and electrochemical impedance measurements were performed by using a Biologic VMP3 multichannel potentiostat (Bio-Logic USA) that was equipped with an external current booster. The i-V measurements were carried out with a 5-mV/s scan rate, and electrochemical impedance was measured between 0.1 and 50 kHz, with a scan rate of 30 points per decade. The direct current (*dc)* and alternating current (*ac)* measurements were performed every 25 h of operation (12).

XRD patterns were obtained simultaneously on all cells before and after the cell operation without any manipulations on the cathode and current collector surfaces. External Al sample holders, Ni/YSZ/GDC ceramic substrates (or YSZ/GDC substrates for symmetric cells), and single-phase PNNO and PrO_x powders were used as external standards to ensure a proper peak positioning and normalized flux. Surface and cross-sectional images on cells were obtained using the Tescan Vega-3 SEM with Energy-dispersive X-ray spectroscopy (EDS) capability. Focused ion beam and EDS analysis was performed on a nano-DUE'T double-beam NB5000 microscope (Hitachi). Elemental mapping on operated electrodes was performed via JEOL 2010F (JEOL Inc.) scanning and transmission electron microscope (STEM) with EDS capability.

Data, Materials, and Software Availability. All study data are included in the main text.

ACKNOWLEDGMENTS. We thank the Department of Energy for the support of this work through Office of Fossil Energy and Carbon Management Grant DE-FE0026097 and Advanced Manufacturing Office of the Office of Energy Efficiency and Renewable Energy Grant DE-EE0009421. This work was also supported by NSF Grant NSF-2119688.

1. H. Schmalzried, W. Laqua, P. L. Lin, Crystalline oxide solid solutions in oxygen potential gradients. *Z. Naturfors.* **34**, 192–199 (1979).
2. D. Dimos, D. L. Kohlstedt, H. Schmalzried, High-temperature creep and kinetic demixing in (Co,Mg)O. *J. Am. Ceram. Soc.* **71**, 732–741 (1988).
3. D. Dimos, D. L. Kohlstedt, Diffusional creep and kinetic demixing in Yttria-stabilized zirconia. *J. Am. Ceram. Soc.* **70**, 531–536 (1987).
4. D. Dimos, J. Wolfenstine, D. L. Kohlstedt, Kinetic demixing and decomposition of multicomponent oxides due to a nonhydrostatic stress. *Acta Metall.* **36**, 1543–1552 (1988).
5. M. Martin, Materials in thermodynamic potential gradients. *J. Chem. Thermodyn.* **35**, 1291–1308 (2003).
6. G. Petot-Ervas, C. Petot, Oxide solid electrolytes under non-equilibrium conditions – Interfaces and ageing. *Ionics* **11**, 189–197 (2005).
7. F. S. Baumann *et al.*, Strong performance improvement of $La_{0.6}Sr_{0.4}Co_{0.8}Fe_{0.2}O_{3\text{-delta}}$ SOFC cathodes by electrochemical activation. *J. Electrochem. Soc.* **152**, A2074–A2079 (2005).
8. H. L. Lein, K. Wiik, T. Grande, Kinetic demixing and decomposition of oxygen permeable membranes. *Solid State Ion.* **177**, 1587–1590 (2006).
9. S. G. Li *et al.*, Tubular lanthanum cobaltite perovskite type membrane for oxygen permeation. *J. Membr. Sci.* **166**, 51–61 (2000).
10. J. E. ten Elshof, H. J. M. Bouwmeester, H. Verweij, Oxidative coupling of methane in a mixed-conducting perovskite membrane reactor. *Appl. Catal. A Gen.* **130**, 195–212 (1995).
11. J. E. ten Elshof, H. J. M. Bouwmeester, H. Verweij, Oxygen transport through $La_{1-x}Sr_xFeO_{3-\delta}$ membranes. 2. Permeation in air/CO, CO_2 gradients. *Solid State Ion.* **89**, 81–92 (1996).
12. E. Dogdibegovic, "Structural, interfacial, and electrochemical properties of Pr2NiO4+δ–based electrodes for solid oxide fuel cells," doctoral dissertation, University of South Carolina, Columbia, SC (2017).
13. E. Dogdibegovic, C. J. Wright, X.-D. Zhou, Stability and activity of, $(Pr1\text{-}xNdx)_2NiO_4$ as cathodes for solid oxide fuel cells. I. Quantification of phase evolution in Pr_2NiO_4. *J. Am. Ceram. Soc.* **99**, 2737–2741 (2016).
14. E. Boehm *et al.*, Oxygen diffusion and transport properties in non-stoichiometric $Ln_{2-x}NiO_{4+d}$ oxides. *Solid State Ion.* **176**, 2717–2725 (2005).
15. T. Broux *et al.*, Structure and reactivity with oxygen of $Pr_2NiO_{(4+\delta)}$: An in situ synchrotron X-ray powder diffraction study. *Dalton Trans.* **45**, 3024–3033 (2016).
16. E. Dogdibegovic, Q. Cai, N. S. Alabri, W. Guan, X.-D. Zhou, Activity and stability of, (Pr1-xNdx)2NiO4 as cathodes for solid oxide fuel cells. III. Crystal structure, electrical properties, and microstructural analysis. *J. Electrochem. Soc.* **164**, F99 (2016).
17. E. Dogdibegovic, Y. Wang, C. J. Wright, X.-D. Zhou, Origin for retained activity in Pr_2NiO_4 while undergoing substantial phase transformation in a long-term solid oxide cell operation. *Nano Energy* **103**, 107684 (2022).
18. E. Dogdibegovic *et al.*, Activity and stability of (Pr1-xNdx)2NiO4 as cathodes for solid oxide fuel cells. Part VI. The role of Cu dopant on the structure and electrochemical properties. *J. Electrochem. Soc.* **164**, F3131–F3139 (2017).
19. E. Dogdibegovic *et al.*, Activity and stability of $(Pr_{1-x}Nd_x)_2NiO_4$ as cathodes for solid oxide fuel cells. Part V. In situ studies of phase evolution. *J. Electrochem. Soc.* **164**, F1115–F1121 (2017).
20. A. V. Virkar, A model for solid oxide fuel cell (SOFC) stack degradation. *J. Power Sources* **172**, 713–724 (2007).
21. A. V. Virkar, "Failure of ion conducting materials by internal precipitation under electrolytic conditions" in *Engineered Ceramics: Current Status and Future Prospects*, T. Ohji, M. Singh, Eds. (The American Ceramic Society and Wiley, Hoboken, NJ, 2016), pp. 59–76.
22. A. V. Virkar, H.-T. Lim, G. Tao, Failure of solid oxide fuel cells by electrochemically induced pressure. *Procedia IUTAM* **10**, 328–337 (2014).
23. H.-T. Lim, A. V. Virkar, A study of solid oxide fuel cell stack failure by inducing abnormal behavior in a single cell test. *J. Power Sources* **185**, 790–800 (2008).
24. E. Ivers-Tiffee, A. Weber, Evaluation of electrochemical impedance spectra by the distribution of relaxation times. *J. Ceram. Soc. Jpn.* **125**, 193–201 (2017).
25. S. Dierickx, A. Weber, E. Ivers-Tiffée, How the distribution of relaxation times enhances complex equivalent circuit models for fuel cells. *Electrochim. Acta* **355**, 136764 (2020).
26. H. Schichlein, A. C. Müller, M. Voigts, A. Krügel, E. Ivers-Tiffée, Deconvolution of electrochemical impedance spectra for the identification of electrode reaction mechanisms in solid oxide fuel cells. *J. Appl. Electrochem.* **32**, 875–882 (2002).
27. S. Lübke, H.-D. Wiemhöfer, Electronic conductivity of Gd-doped ceria with additional Pr-doping. *Solid State Ion.* **117**, 229–243 (1999).
28. E. Dogdibegovic *et al.*, The role of interlayer on the catalytic activity and performance stability of $(Pr_{1-x}Nd_x)_2NiO_4$ as cathodes for solid oxide fuel cells. *ECS Trans.* **78**, 983–992 (2017).
29. Y. Zhang *et al.*, Role of Pr-vacancies and O-interstitials on the activity and stability of $(Pr_{1-x}Ln_x)_2NiO_4$ (Ln= La, Nd, Pm, Sm, Gd, Tb, Dy, and Ho) towards oxygen reduction reactions: A DFT study. *J. Electrochem. Soc.* **168**, 124508 (2021).
30. L. A. Chick *et al.*, Glycine-nitrate combustion synthesis of oxide ceramic powders. *Mater. Lett.* **10**, 6–12 (1990).
31. E. Dogdibegovic, W. Guan, J. Yan, M. Cheng, X.-D. Zhou, Activity and stability of, (Pr1-xNdx)2NiO4 as cathodes for solid oxide fuel cells. II. Electrochemical performance and performance durability. *J. Electrochem. Soc.* **163**, F1344–F1349 (2016).